Journal of Alloys and Compounds 992 (2024) 174554

Contents lists available at ScienceDirect

Journal of Alloys and Compounds

journal homepage: www.elsevier.com/locate/jalcom

Decoding the oxidation mechanism of Zircaloy-4 via *in situ* synchrotron X-ray diffraction and computational elucidation

Shubo Wang [a,*], Leran Lu [a], Al Rahemtulla [b], Marko Huttula [a], Martin Steinbrück [c,*], Harishchandra Singh [a]

[a] Nano and Molecular Systems Research Unit, University of Oulu, Oulu 90570, Finland
[b] Canadian Light Source, 44 Innovation Blvd., Saskatoon, Saskatchewan S7N 2V3, Canada
[c] Karlsruhe Institute of Technology, Institute for Applied Materials, IAM-AWP, Karlsruhe, Germany

ARTICLE INFO

Keywords:
Zircaloy-4
Oxidation
In situ synchrotron X-ray diffraction
DFT computation

ABSTRACT

Comprehensive understanding of the oxidation behavior of Zr alloys, a vital cladding material in nuclear power plants, is essential for developing improved materials and enhancing the safety and performance of nuclear systems. Herein, the bulk oxidation behavior in ambient air atmosphere of Zircaloy-4 were revisited through *in situ* synchrotron X-ray diffraction and DFT computation. The results reveal the phase transition sequences at a representative 900 °C oxidation temperature: hcp Zr recrystallizes rapidly and then transforms into bcc Zr while reaching the α+β transus, followed by speedy appearance of textured tetragonal (t-)ZrO_2, monoclinic (m-)ZrO_2 and ZrN that consume oxygen and nitrogen. Continuous air ingress favors t-ZrO_2 and m-ZrO_2 dominance, accompanied by re-oxidation of ZrN into t-ZrO_2 due to its low thermodynamic stability revealed by experiment-informed DFT calculation and low oxygen activity at the oxide-metal interface. Ensemble-averaged lattice volume expansions during phase transitions have been quantified. This expansion-induced compressive stress promotes the presence of a significant fraction of t-ZrO_2 at elevated temperature that eventually transforms into m-ZrO_2 during cooling.

1. Introduction

Zirconium (Zr) alloys have been used worldwide in nuclear power industries as fuel claddings due to their endurability in harsh application conditions which require excellent corrosion and mechanical properties, and more importantly, low neutron absorption cross-section [1]. During hypothetic nuclear power plant accidents that are indeed of very low probability, high temperature oxidation of Zr alloys by air and air-steam mixed atmospheres is very likely to result in serious degradation of claddings and release of fission products, which potentially have very severe consequences [2]. Despite that it has been intensively proposed to replace Zr alloys by more advanced materials with optimized oxidation resistance and properties [3,4], Zr alloys still prevail owing to their exceptionally low neutron cross section. The most promising alternative is to implement either protective coatings that are more durable in the corrosive nuclear reactor environment [5–7]. Nevertheless, the key challenges in the adoption of coating are inadequate adhesion with Zr alloy substrates and potential cracks after irradiation creep and growth [3,8]. In turn, Zr alloy claddings still suffer oxidation.

During hypothetical accidental situations, Zr alloy claddings are exposed to not only high temperature oxidation in possibly various atmospheres and but also quenching due to core reflooding [9,10]. There are extensive studies carried out examining the oxidation kinetics of Zr alloys at high-temperature air and air-steam mixture environments, for example in [11–18]. The obtained kinetic data are generally consistent well with each other: oxidation in air-steam mixture is more severe than in steam only but varies with air/steam mixing ratio and temperature; and oxidization rate in air is generally comparable to, or even faster than that in air-steam mixture. Additionally, research efforts have increasingly focused on air ingress degradation scenarios [17–20], after the Fukushima accidents. On the other hand, detailed microstructural analyses, especially *in situ* measurement, of the oxidation products, sequences of Zr to ZrO_2 phase transformations are less reported. Generally, the growth of zirconia scale on the surface of Zr alloys is due to solid-state diffusion of oxygen. In atmospheric air, nitridation could also take place [19,21]. The structure of oxide layers depends significantly

* Corresponding authors.
E-mail addresses: shubo.wang@oulu.fi (S. Wang), martin.steinbrueck@kit.edu (M. Steinbrück).

https://doi.org/10.1016/j.jallcom.2024.174554
Received 8 February 2024; Received in revised form 17 April 2024; Accepted 18 April 2024
Available online 21 April 2024

on oxidation temperatures, *i.e.*, tetragonal (t-) ZrO_2 at high temperature above 1100 °C, mixture of t- and monoclinic (m-) ZrO_2 at intermediate temperature range, and then mainly m-ZrO_2 below 900 °C [22,23]. Drawn conclusions are mainly based on post-mortem structural characterizations and/or surface characterization techniques [21–23]. It means that exiting data regarding the structural complexity of solid-state phase transformations within bulk Zr alloy and oxide layer are scarcely reported.

Herein, we adopted *in situ* synchrotron X-ray diffraction (SXRD), a non-destructive technique for studying and statistically quantifying microstructural features in materials [24,25], to investigate the structural evolutions during oxidation of a common Zircaloy-4 cladding material in air. The oxidation temperature was chosen to be at 900 °C that is a typical median value in most of the publications and in hypothetic accident scenarios, for instance in spent fuel pools [26]. We also combine quantitative analysis of *in situ* SXRD results with experimental data informed density functional theory (DFT) computations to revisit and to elucidate the oxidation mechanism.

2. Experimental

A commercial Zircaloy-4 cladding tube (10.75 mm external diameter, 0.75 mm thickness) was employed and machined into segments with a dimension of 0.9 × 0.75 × 15 mm^3 along the tube's longitudinal direction. *In situ* SXRD measurement using monochromatic X-ray beam ($\lambda = 0.1779$ Å) was performed in a transmission mode at the Brockhouse High Energy Wiggler Beamline [27], Canadian Light Source, Canada. The rod segments were heated at a rate of 10 °C/s using a flow-cell furnace [28] under natural air convection to simulate possible air ingress accident scenarios. Therefore, oxidation occurred on all the free surface of the employed sample. Raw SXRD patterns were collected in a stepwise manner during the heating to 900 °C and cooling cycle, where the temperature was held at each step (every 100 °C and every 30 min during holding at 900 °C) for 60 s for data recording. Here, the exposure time was 1 s, and 10 snapshots were acquired to optimize the data collection and to ensure a reasonable statistic. The acquired 2D diffraction patterns were integrated into 1D profiles by GSAS-II [29]. Quantitative phase weight fractions are calculated by applying the RIR method to resulting profiles [30].

The formation energy (E_f) was calculated using:

$$E_f = \frac{E_{tot} - \sum n_i \mu_i}{N} \quad (1)$$

where E_{tot} is the system's total energy, n_i is the number of atoms of element i in the structure of interest, μ_i is the energy of a single atom of element i when it is in its most stable simple substantial form, N is the total number of atoms in the system, respectively. To calculate E_f of the structure at elevated temperatures, the shape and volume of considered unit cells were frozen in DFT calculations, which was contrary to the relaxed ground-state structure calculations at absolute 0 K where all the lattice parameters were optimized. All the calculations were conducted in the framework of DFT implemented in the Vienna *ab initio* simulation package (VASP) [31]. The Perdew-Burke-Ernzerhof (PBE) exchange-correlation functional under the generalized gradient approximation (GGA) [32] was applied. A cutoff energy of 520 eV was adopted for the plane wave basis set. The Γ-centered scheme k-mesh generated by VASPKIT [33] with a spacing value of 0.04 in unit of $2\pi \cdot Å^{-1}$ was used. To simulate vacancies and substitutional nitrogen atoms that were believed to stabilize the metastable t-ZrO_2 structure [34], 2 × 2 × 2 supercells were generated using the open-source Transformer code [35] by enumerating all the symmetry-inequivalent structures and degeneracies built by successively introducing vacancies in the supercells. We intentionally set the vacancies and substitutional atoms at O sites to be 4 % [36] to simplify the calculations. This yielded 2367 unique structures in 15 distinct configurations, respectively, among which only 10 were picked randomly for the calculation of formation energy.

3. Results and discussion

Experimental SXRD profiles for the starting and finishing material and simulated powder diffraction spectra for phases that could present in the material based on the well-established Zr-O and Zr-N phase diagrams [37,38] are shown in Fig. 1a. At room temperature (RT), diffraction peaks of the starting material correspond well to the lattice plane reflections of hexagonal close packed (hcp) α-Zr (PDF 04–008–1477). A clear basal texture is seen, as the intensity ratio of (0002) to $(10\bar{1}1)$ peak is much higher than that of its powder counterpart given in Table S1. This anisotropic phenomenon is representative in such Zr alloys, which is attributed to the hcp crystals that deformed by both slip and twinning mechanisms to develop a strong texture during cold working in order to enhance the yield strength [39,40]. The final products after oxidation at 900 °C for 2 h consist of mainly m-ZrO_2 (space group of P21/c, PDF 01–070–2491) with a few t-ZrO_2 (space group of P42/nm, PDF 01–070–6627). Thanks to the high resolution of synchrotron X-ray, we do not observe the presence of high temperature cubic polymorph of ZrO_2 or zirconium oxynitrides $ZrO_{2-2x}N_{4x/3}$ as in [23]. Nevertheless, a subtle peak asymmetry at 2θ around 3.89° and peak splitting around 4.45° (inset of Fig. 1a) gives a hint of the presence of minor ZrN (PDF 00–035–0753).

Comparing with the high temperature spectra shown in Fig. 1b, it is clear that the post-mortem observations cannot represent the phase transitions that occurred in bulk Zr alloys during high temperature oxidation. The intensity ratio of (0002) to $(10\bar{1}1)$ peak for α-Zr decreases with increase in temperature before 900 °C, indicating the occurrence of recrystallization [40] at the expense of initial cold worked components. It is further supported by the 2D diffraction pattern where the Debye-Scherrer rings for α-Zr at initial RT turn into scattered diffraction spots (Fig. S1). Observation of the diffractograms at 800 and 900 °C demonstrates that the onset of hcp to bcc (body centered cubic β-Zr, PDF 04–004–9112) transformation occurs, evidenced by the most distinguishable and intense (110) reflection for β-Zr located between α-Zr (0002) and $(10\bar{1}1)$ reflections. Simultaneous appearance of m- and t-ZrO_2 is clearly visible after 30 min oxidation at 900 °C. Dominant phase constituents are still metallic α- and β-Zr after 60 min oxidation, and then change completely to zirconia after 90 min. During cooling, t-ZrO_2 is seen transforming to m-ZrO_2. Ideally, at room temperature, intensity ratio of (111) at 3.578° to $(11\bar{1})$ peak at 3.220° for m-ZrO_2 should be 71.6 % in Table 1. However, the experimental data displays 79 %, indicating that the oxidation products also have preferred crystal orientations. This is an interesting finding, which might related with the strong texture and texture memory effect in such Zr alloys [41].

Quantitative determinations, summarized in Fig. 2, are necessary to fully unveil the phase fractions characterized by these diffraction peaks. Owing to the presented texture and peak overlapping at high 2θ angle range, we limited our interests in a 2θ range from 2.5° to 5° covering the most intensive peaks for all the phases summarized in Fig. 1a. During rapid heat ramp from 800 to 900 °C, hcp to bcc transformation occurs prior to any oxidation. It is noticeable that the ratio between α- and β-Zr maintains roughly 1:1 before full oxidation, representing the α+β region with 50 % β-Zr at 900 °C. The Zr lattice could tolerate up to about 30 at % O or N at 900 °C to stabilize the hcp α crystal structure [37,38], resulting in more α-Zr in this work compared with [42]. Thus, O_2 and/or N_2 uptake at the metal-air interface firstly occurs:

$$2(\alpha/\beta)\text{-Zr} + O_2/N_2 \rightarrow 2\alpha\text{-Zr(O/N)} \quad (2)$$

Holding at 900 °C for just about 1 min results in a small fraction (~2.5 wt %) of co-existing t- and m-ZrO_2, marking the initiation of newly formed oxide at the surface of bulk sample. The presence of ZrN is barely detectable, which might be due to the surface to bulk diffusion coefficient of N_2 is lower than O_2 (Fig. S2) [43]. After continuous

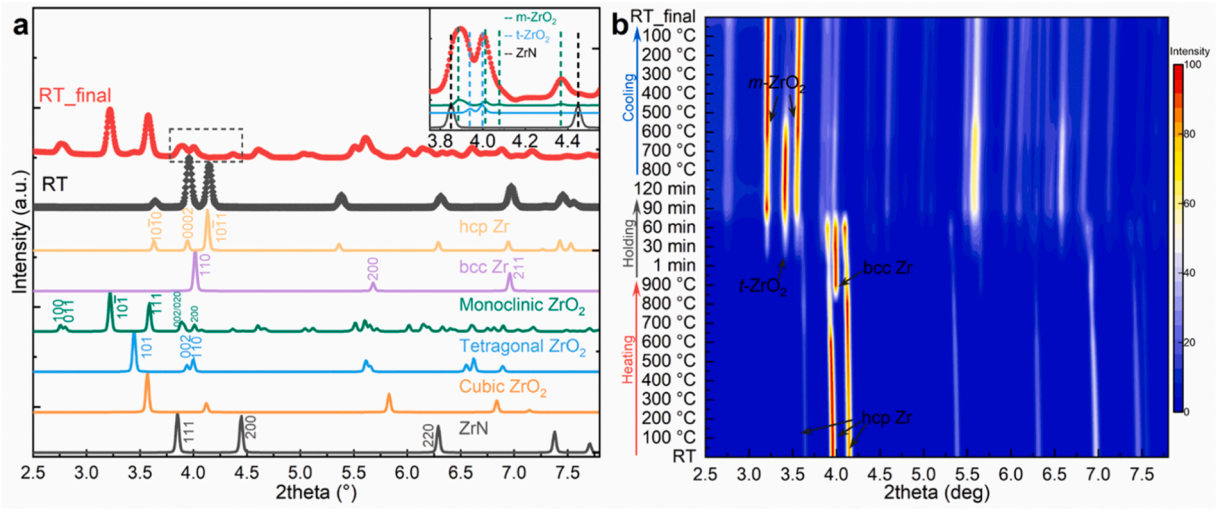

Fig. 1. SXRD profiles of Zircaloy-4 sample. (a) Comparison between room temperature SXRD profiles (scatters) and single-phase power diffraction pattern (solid lines). (b) Contour plot for all profiles as a function of the heating-cooling cycle. The intensity values of the profiles were normalized using min-max scaling method. Inset of (a) depicts the presence of minor ZrN phase results in the asymmetric peak at around 3.89° owing to $(111)_{ZrN}$ reflections and 'shoulder' hump around 4.45° owing to $(200)_{ZrN}$ reflections, in which the colored dash lines highlight the peak positions of different phases.

Table 1
Lattice parameters (*a, b, c* in Å) of phases involved in the oxidization of investigated Zircaloy-4 alloy. Number in parentheses represents the uncertainties on the last digit of the corresponding calculated lattice parameter.

	hcp α-Zr	bcc β-Zr	t-ZrO_2	m-ZrO_2	ZrN
RT	a =3.2301(1) c =5.1520(1)				
900 °C	a = 3.2477(2) c = 5.2120(2)	a = 3.6096(2)	a =3.6390(2) c =5.2310(2)	a =5.1866(1) b = 5.2155(2) c = 5.3765(1)	a = 4.6140(2)
RT_f			a = 3.5908(2) c = 5.2192(2)	a = 5.1594(1) b = 5.2207(1) c = 5.3265(1)	a = 4.5850(2)

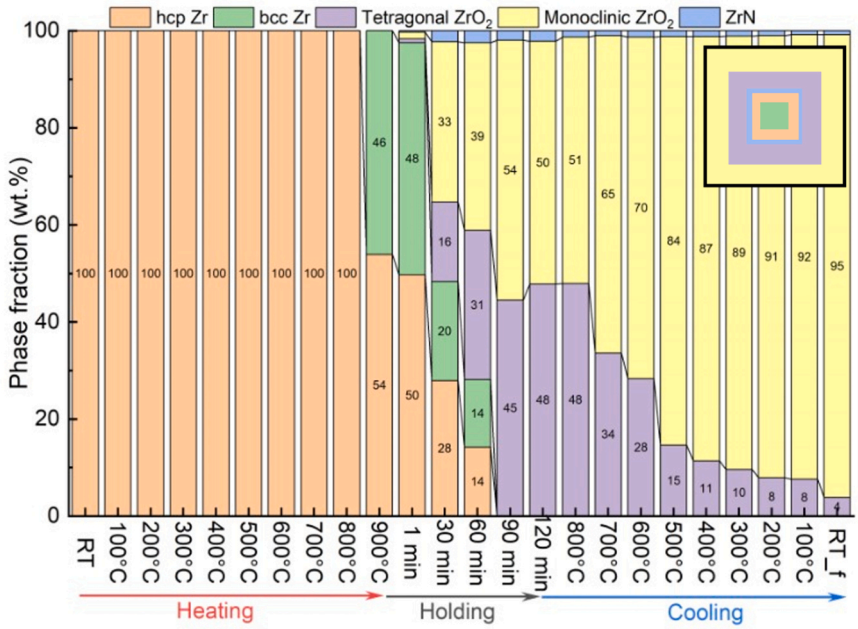

Fig. 2. Weight fraction of phases during the heating and cooling cycles, estimated by quantitative analysis of SXRD patterns. The inset drawing schematically shows the cross-sectional distribution of phases in the Zircaloy. Areas in the inset drawing do not represent the actual phase fractions.

oxidation for 30 min, both t- and m-ZrO_2 increase significantly along with a small fraction (~ 2.3 wt %) of ZrN. The increment of t-ZrO_2 is more than m-ZrO_2, deviating from grazing incident XRD observations in [22] where only a very shallow surface layer was probed. Therefore, it can be concluded that t-ZrO_2 presents more inward than m-ZrO_2, meaning that the oxygen diffusion inwards across existing oxide layer leads to the formation of t-ZrO_2 at the metal-oxide interface firstly at 900 °C. The presence of m-ZrO_2 at outer layer is owing to the inner-layer t-ZrO_2 to m-ZrO_2 transition. Consequently, we can conclude that O_2 and N_2 is further consumed by these reactions,

$$2Zr(O/N) + O_2 \rightarrow t\text{-}ZrO_2 \quad (3)$$

$$2Zr(O/N) + N_2 \rightarrow 2ZrN \quad (4)$$

respectively:

To access the thermodynamical behavior of metallic Zr, we calculated the stability of phases in the form of formation energy E_f in Fig. 3, employing the experimentally obtained structural information (Table 1) of the product phases at 900 °C for 30 min. Reliability of the associated calculations [25] were validated by comparing the total energy E_{tot} of an optimized structure from experimentally obtained results at ground state with these in database [44], which reveals only a small deviation ≤ 1 % (Table S2). Specifically, we also introduce O deficiency and N dopants for t-ZrO_2, as it is frequently reported that metastable t-ZrO_2, mainly in powder form for catalytic reactions, can be stabilized by introducing O deficiency [34] and dopants [45,46]. Positive E_f values are seen for metallic α- and β-Zr, while negative values for ZrO_2 and ZrN phases, hence, oxidation occurs. The E_f of t- and m-ZrO_2 appears to be much lower than that for ZrN, following the order of $E_{f,m\text{-}ZrO_2} < E_{f,t\text{-}ZrO_2} < E_{f,t\text{-}ZrO_{2-\delta}} < E_{f,t\text{-}ZrO(xN)_{2-\delta}} \ll E_{f,ZrN}$. ZrN is the least energetically favourable species. However, oxygen activity is low enough for ZrN to from typically at the metal-oxide interface [47], suggesting that Eq. 4 could take place competitively, simultaneously, or even early than Eq. 3. As the reactions, Eqs. 3 and 4, progress, ZrN moves away from the metal-oxide interface to oxide matrix where the oxygen activity increases to re-oxidize ZrN to ZrO_2 owing to its low thermodynamic stability:

$$2ZrN + 2O_2 \rightarrow 2t\text{-}ZrO_2 + N_2 \quad (5)$$

This reaction has been experimentally observed to be a strong exothermic reaction [48,49], consistent with calculated E_f. It is associated with a ~41 % increase in volume of ZrN to t-ZrO_2 according to Table 1.

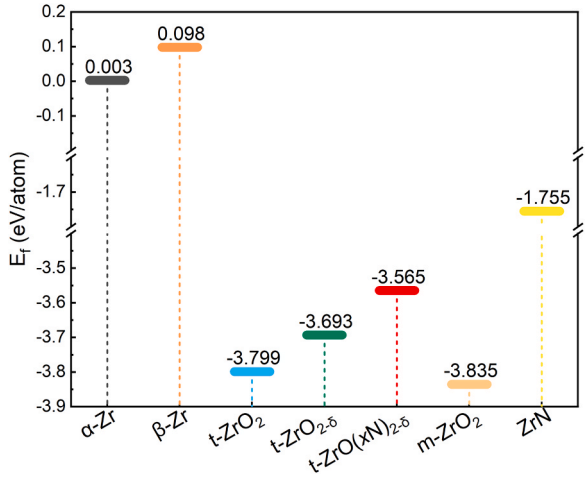

Fig. 3. Thermal-related DFT calculated formation energy (E_f) for metallic Zr (α/β), ZrN, t-ZrO_2, vacancy-containing t-$ZrO_{2-\delta}$, N doped t-$ZrO(xN)_{2-\delta}$ and m-ZrO_2. Regarding the metastable tetragonal ZrO_2, oxygen deficiency was taken as roughly δ = 4 %, referring to [34].

m-ZrO_2 is the most stable species and supposed to be predominant compared with t-ZrO_2 and ZrN. According to the zirconia phase diagram, the t- to m-ZrO_2 transition is martensitic type, which occurs around 1100 °C and then completes at around 900 °C [50]. However, a greater increment of t-ZrO_2 and nearly constant fraction of ZrN are detected in our work despite of the concurrent t- to m-ZrO_2 transition (Fig. 2), ascertaining i) the occurrence of Eqs. 3 and 4 for the mitigation of oxidation front, ii) that the formation of only-interfacial but thermodynamically unstable ZrN (Eq. 4) is ascribed to low oxygen activity as in [47], and iii) that the formation of metastable t-ZrO_2 is very likely due to oxygen starvation. As a diffusion-controlled reaction observed by the parabolic kinetics in [11–16,18], t-ZrO_2 dynamically transforms into m-ZrO_2 due to their intrinsic thermodynamic stabilities and oxygen uptake with increase in surrounding oxygen abundance by continuous air ingress:

$$t\text{-}ZrO_{(2-x)} + 2/xO_2 \rightarrow m\text{-}ZrO_2 \quad (6)$$

Hence, from the inner centre towards surface, the order of stacked phases is: β-Zr | α-Zr(O/N) | ZrN incorporated t-ZrO_2 layer | m-ZrO_2, as schematically shown in the inset of Fig. 2.b.

The cooling cycle causes continuous t- to m-ZrO_2 transition as the metallic Zr has been consumed completely. It is believed that this transition especially during cooling leads to significant volume increment and built compressive stress owing to the volume and thermal expansion coefficient mismatches in Zr, ZrN, t- and m-ZrO_2 [51,52]. Such stress is relieved by the formation of lateral cracks within the ZrO_2 scales and at center of the rod (Fig. 4b,e *vs* a,c), and subsequently breakaway of ZrO_2 scales (Fig. S3), revealing a roughly isotropic oxidation. Failure of zircaloy based claddings, thus, is just there.

Color of the sample's surface shows a rich yellow color (Fig. S3), which is the same color (light yellowish) observed using normal indoor lighting illumination as previous result [53]. Post-mortem SEM characterization on another set of samples oxidized in muffle furnace at 900 °C for 20 min was also performed. Thickness of the oxide layer, with wavy front and interior lateral cracks (Fig. 4d1), is measured to be roughly 20 μm, agrees well with [54]. This layer is dominated by m-ZrO_2 with poor conductivity (surface charging in the image) through t- to m-ZrO_2 transition, as evidenced by above *in situ* study. Stress is partially relaxed in this region by quite large crack generation, while smaller-scale micropores and cracks are observed in the thinner region that consists of mainly t-ZrO_2 and ZrN at the oxide-metal interface (Fig. 4d2). It is frequently believed that the layer has high compressive stress [55–59] that contributes to stabilize t-ZrO_2 despite of its intrinsic metastability revealed by lower E_f. Herein, from the unveiled sequence of stacked phase by SXRD quantification (Table 1), the ensemble-averaging volume expansions, as sources stress, due to the listed reactions (Eqs. 2–6) are calculated to be i) 1.3 % by α-Zr to β-Zr then back to α-Zr(O,N) transition occurring within the metallic matrix (Eq. 2), ii) 45.5 % by Zr oxidation to t-ZrO_2, (Eq. 3), iii) 3.2 % by formation ZrN (Eq. 4), iv) 41 % by ZrN re-oxidation (Eq. 5), and v) 4.0 % due to t- to m-ZrO_2 transition (Eq. 6). The overall expansion is 51 % from Zr to final product m-ZrO_2.

4. Conclusion

Using *in situ* SXRD and DFT computation, the oxidation behavior of a nuclear cladding material, Zircaloy-4 in air, was explored in this work. During a rapid heating/cooling cycle that simulates the low-probability nuclear plant accident, the hcp Zr recrystallizes and then transforms to bcc Zr first. Experimental results informed DFT calculation shows the zirconia and ZrN phases are more energetically favorable at 900 °C. Therefore, t- and m-ZrO_2 form rapidly and simultaneously, which deviates from the phase diagrams and previous reports. As the oxidation duration extends at 900 °C with continuous air ingress, t- and m-ZrO_2 become predominant through the simultaneous Zr and O_2 reaction and

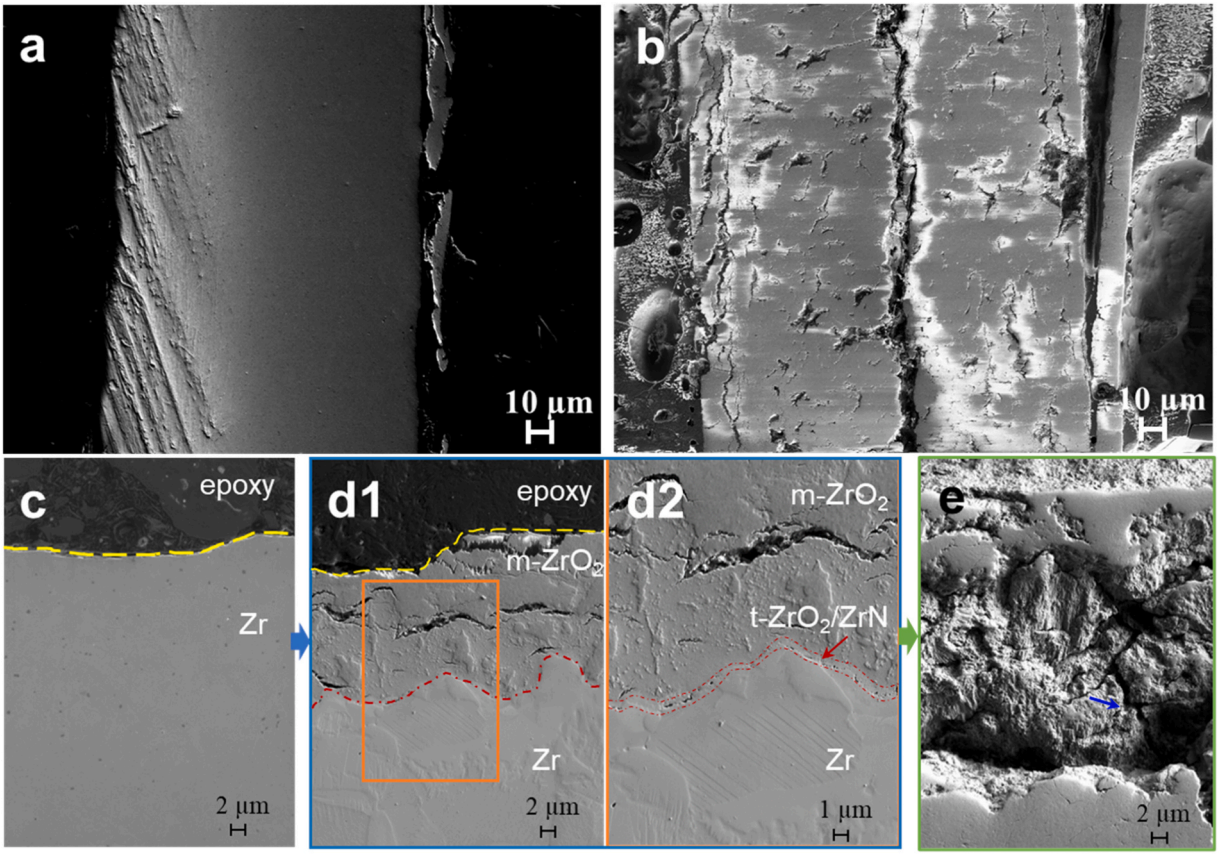

Fig. 4. SEM cross-sectional images of Zircaloy-4 alloy sample before (a, c) oxidation and after oxidation at 900 °C for (d) 30 min and (b, e) 2 h, respectively. Yellow and red dashed lines denote the interface between sample and supporting epoxy, interface between ZrO_2 and α-Zr(O) metallic region.

t- to m- ZrO_2 phase transition. Nitrogen in the air is consumed by the formation of ZrN. However, ZrN can be re-oxidized into t-ZrO_2 which occurs mainly oxide-metal interface, owing to its low thermodynamic stability compared with zirconia. The obtained lattice parameter for various phases gives roughly 1.3 % volume expansion for the metallic Zr transitions in the central layer and about 4.0 % for t- to m-ZrO_2 transition in the outer layer, but more than 40 % by formation of t-ZrO_2 via direct oxidation of Zr and re-oxidation of ZrN. Such compressive stress facilitates the presence of a large fraction of t-ZrO_2 in the intermediate layer at elevated temperatures which eventually transforms to m-ZrO_2 during the cooling stage.

CRediT authorship contribution statement

Shubo Wang: Writing – original draft, Formal analysis, Data curation, Conceptualization. **Leran Lu:** Methodology, Formal analysis, Data curation. **Harishchandra Singh:** Initialization and planning, Writing – review & editing, Validation, Supervision, Methodology, Investigation, Conceptualization. **Martin Steinbruck:** Writing – review & editing, Validation, Supervision, Resources. **Marko Huttulla:** Writing – review & editing, Supervision, Resources, Funding acquisition. **Al Rahemtulla:** Methodology.

Declaration of Competing Interest

The authors declare that they have no known competing financial interests or personal relationships that could have appeared to influence the work reported in this paper.

Data Availability

Data will be made available on request.

Acknowledgments

SW thanks Dr. Romain Botella for interesting discussions. Sample preparation by Mr. Tun Tun Nyo and Dr. Sumit Ghosh at University of Oulu is greatly appreciated by the authors. Computational resources were provided by CSC-IT Center for Science, Finland. Part of the work was carried out with the support of the Centre for Material Analysis, University of Oulu, Finland. Authors thank Dr. Graham King for the assistance during synchrotron data collection. Part of the research described in this work was performed at the Canadian Light Source, a national research facility of the University of Saskatchewan, which is supported by the Canada Foundation for Innovation (CFI), the Natural Sciences and Engineering Research Council (NSERC), the National Research Council (NRC), the Canadian Institutes of Health Research (CIHR), the Government of Saskatchewan, and the University of Saskatchewan. HS thanks Jane ja Aatos Erkon säätiö (JAES) and Tiina ja Antti Herlinin säätiö (TAHS) for the financial supports on Advanced Steels for Green Planet project. The work is also supported by Strategic Research Council within the Research Council of Finland decision 358422, JustH2Transit.

Appendix A. Supporting information

Supplementary data associated with this article can be found in the online version at doi:10.1016/j.jallcom.2024.174554.

References

[1] S.J. Zinkle, G.S. Was, Materials challenges in nuclear energy, Acta Mater. 61 (2013) 735–758, https://doi.org/10.1016/j.actamat.2012.11.004.

[2] B. Cox, Some thoughts on the mechanisms of in-reactor corrosion of zirconium alloys, J. Nucl. Mater. 336 (2005) 331–368, https://doi.org/10.1016/j.jnucmat.2004.09.029.

[3] T. Nozawa, T. Koyanagi, Y. Katoh, H. Tanigawa, Failure evaluation of neutron-irradiated SiC/SiC composites by underwater acoustic emission, J. Nucl. Mater. 566 (2022) 153787, https://doi.org/10.1016/j.jnucmat.2022.153787.

[4] K.A. Terrani, S.J. Zinkle, L.L. Snead, Advanced oxidation-resistant iron-based alloys for LWR fuel cladding, J. Nucl. Mater. 448 (2014) 420–435, https://doi.org/10.1016/j.jnucmat.2013.06.041.

[5] R.V. Umretiya, S. Vargas, D. Galeano, R. Mohammadi, C.E. Castano, J.V. Rojas, Effect of surface characteristics and environmental aging on wetting of Cr-coated Zircaloy-4 accident tolerant fuel cladding material, J. Nucl. Mater. 535 (2020) 152163, https://doi.org/10.1016/j.jnucmat.2020.152163.

[6] M. Slobodyan, High-energy surface processing of zirconium alloys for fuel claddings of water-cooled nuclear reactors, Nucl. Eng. Des. 382 (2021) 111364, https://doi.org/10.1016/j.nucengdes.2021.111364.

[7] C. Tang, M. Stueber, H.J. Seifert, M. Steinbrueck, Protective coatings on zirconium-based alloys as accident-tolerant fuel (ATF) claddings, Corros. Rev. 35 (2017) 141–165, https://doi.org/10.1515/corrrev-2017-0010.

[8] C. Meng, L. Yang, Y. Wu, J. Tan, W. Dang, X. He, X. Ma, Study of the oxidation behavior of CrN coating on Zr alloy in air, J. Nucl. Mater. 515 (2019) 354–369, https://doi.org/10.1016/j.jnucmat.2019.01.006.

[9] M. Steinbrück, M. Große, L. Sepold, J. Stuckert, Synopsis and outcome of the QUENCH experimental program, Nucl. Eng. Des. 240 (2010) 1714–1727, https://doi.org/10.1016/j.nucengdes.2010.03.021.

[10] R. Gharari, H. Kazeminejad, N. Mataji Kojouri, A. Hedayat, A review on hydrogen generation, explosion, and mitigation during severe accidents in light water nuclear reactors, Int. J. Hydrog. Energy 43 (2018) 1939–1965, https://doi.org/10.1016/j.ijhydene.2017.11.174.

[11] M. Steinbrück, J. Birchley, A.V. Boldyrev, A.V. Goryachev, M. Grosse, T.J. Haste, Z. Hózer, A.E. Kisselev, V.I. Nalivaev, V.P. Semishkin, L. Sepold, J. Stuckert, N. Vér, M.S. Veshchunov, High-temperature oxidation and quench behaviour of Zircaloy-4 and E110 cladding alloys, Prog. Nucl. Energy 52 (2010) 19–36, https://doi.org/10.1016/J.PNUCENE.2009.07.012.

[12] M. Steinbrück, M. Böttcher, Air oxidation of Zircaloy-4, M5® and ZIRLO™ cladding alloys at high temperatures, J. Nucl. Mater. 414 (2011) 276–285, https://doi.org/10.1016/j.jnucmat.2011.04.012.

[13] M. Steinbrück, Oxidation of zirconium alloys in oxygen at high temperatures up to 1600 °C, Oxid. Met. 70 (2008) 317–329, https://doi.org/10.1007/s11085-008-9124-z.

[14] A.R. Singh, B. Puranik, O. Gokhale, D. Mukhopadhyay, Effects of elevated temperature steam oxidation and subsequent quenching on light water reactor clad, Prog. Nucl. Energy 155 (2023) 104510, https://doi.org/10.1016/j.pnucene.2022.104510.

[15] Y. Nemoto, Y. Ishijima, K. Kondo, Y. Fujimura, Y. Kaji, Investigation of the oxidation behavior of Zircaloy-4 cladding in a mixture of air and steam, J. Nucl. Mater. 575 (2023) 154209, https://doi.org/10.1016/j.jnucmat.2022.154209.

[16] C. Duriez, T. Dupont, B. Schmet, F. Enoch, Zircaloy-4 and M5® high temperature oxidation and nitriding in air, J. Nucl. Mater. 380 (2008) 30–45, https://doi.org/10.1016/j.jnucmat.2008.07.002.

[17] C. Duriez, D. Drouan, G. Pouzadoux, Reaction in air and in nitrogen of pre-oxidised Zircaloy-4 and M5™ claddings, J. Nucl. Mater. 441 (2013) 84–95, https://doi.org/10.1016/j.jnucmat.2013.04.095.

[18] M. Lasserre, V. Peres, M. Pijolat, O. Coindreau, C. Duriez, J. -P. Mardon, Qualitative analysis of Zircaloy-4 cladding air degradation in O 2 –N 2 mixtures at high temperature, Mater. Corros. 65 (2014) 250–259, https://doi.org/10.1002/maco.201307078.

[19] L. Kurpaska, I. Jozwik, J. Jagielski, Study of sub-oxide phases at the metal-oxide interface in oxidized pure zirconium and Zr-1.0% Nb alloy by using SEM/FIB/EBSD and EDS techniques, J. Nucl. Mater. 476 (2016) 56–62, https://doi.org/10.1016/j.jnucmat.2016.04.038.

[20] W. Zhao, T. Wei, J. Liao, P. Song, X. Peng, Z. Liao, Q. Peng, X. He, High-temperature oxidation behavior of Zr-4 and Zr-Sn-Nb alloy in different oxidation ambient, J. Alloy. Compd. 887 (2021) 161396, https://doi.org/10.1016/j.jallcom.2021.161396.

[21] J.L. Vandegrift, P.M. Price, J.P. Stroud, C.J. Parga, I.J. Van Rooyen, B.J. Jaques, D. P. Butt, Oxidation behavior of Zirconium, Zircaloy-3, Zircaloy-4, Zr-1Nb, and Zr-2.5 Nb in air and oxygen, Nucl. Mater. Energy 20 (2019) 100692, https://doi.org/10.1016/j.nme.2019.100692.

[22] D. Gosset, M. Le Saux, D. Simeone, D. Gilbon, New insights in structural characterization of zirconium alloys oxidation at high temperature, J. Nucl. Mater. 429 (2012) 19–24, https://doi.org/10.1016/j.jnucmat.2012.05.003.

[23] I. Idarraga, M. Mermoux, C. Duriez, A. Crisci, J.P. Mardon, Raman investigation of pre- and post-breakaway oxide scales formed on Zircaloy-4 and M5® in air at high temperature, J. Nucl. Mater. 421 (2012) 160–171, https://doi.org/10.1016/j.jnucmat.2011.11.071.

[24] S. Ghosh, S. Wang, H. Singh, G. King, Y. Xiong, T. Zhou, M. Huttula, J. Kömi, W. Cao, Quantitative prediction of yield strength of highly alloyed complex steel using high energy synchrotron X-ray diffractometry, J. Mater. Res. Technol. 20 (2022) 485–495, https://doi.org/10.1016/j.jmrt.2022.07.066.

[25] S. Wang, A.A. Kistanov, G. King, S. Ghosh, H. Singh, S. Pallaspuro, A. Rahemtulla, M. Somani, J. Kömi, W. Cao, M. Huttula, In-situ quantification and density functional theory elucidation of phase transformation in carbon steel during quenching and partitioning, Acta Mater. 221 (2021) 117361, https://doi.org/10.1016/j.actamat.2021.117361.

[26] J. Martin, N. Trégourès, OECD/NEA R&D priorities for loss-of-cooling and loss-of-coolant accidents in Spent-Fuel-Pools, Nucl. Eng. Des. 410 (2023) 112380, https://doi.org/10.1016/j.nucengdes.2023.112380.

[27] A. Gomez, G. Dina, S. Kycia, The high-energy x-ray diffraction and scattering beamline at the Canadian Light Source, Rev. Sci. Instrum. 89 (2018) 063301, https://doi.org/10.1063/1.5017613.

[28] B. Zhang, J. Wang, B. Wu, Y.T. Zhou, X.L. Ma, Quasi-in-situ ex-polarized TEM observation on dissolution of MnS inclusions and metastable pitting of austenitic stainless steel, Corros. Sci. 100 (2015) 295–305, https://doi.org/10.1016/J.CORSCI.2015.08.009.

[29] B.H. Toby, R.B. Von Dreele, GSAS-II: the genesis of a modern open-source all purpose crystallography software package, J. Appl. Crystallogr. 46 (2013) 544–549, https://doi.org/10.1107/S0021889813003531.

[30] H. Toraya, A new method for quantitative phase analysis using X-ray powder diffraction: direct derivation of weight fractions from observed integrated intensities and chemical compositions of individual phases, J. Appl. Crystallogr. 49 (2016) 1508–1516, https://doi.org/10.1107/S1600576716010451.

[31] G. Kresse, J. Furthmüller, Efficient iterative schemes for ab initio total-energy calculations using a plane-wave basis set, Phys. Rev. B - Condens. Matter Mater. Phys. 54 (1996) 11169–11186, https://doi.org/10.1103/PhysRevB.54.11169.

[32] J.P. Perdew, K. Burke, M. Ernzerhof, Generalized gradient approximation made simple, Phys. Rev. Lett. 77 (1996) 3865–3868, https://doi.org/10.1103/PhysRevLett.77.3865.

[33] V. Wang, N. Xu, J.C. Liu, G. Tang, W.T. Geng, VASPKIT: a user-friendly interface facilitating high-throughput computing and analysis using VASP code, Comput. Phys. Commun. 267 (2021) 108033, https://doi.org/10.1016/j.cpc.2021.108033.

[34] M. Yashima, S. Tsunekawa, Structures and the oxygen deficiency of tetragonal and monoclinic zirconium oxide nanoparticles, Acta Crystallogr. Sect. B Struct. Sci. 62 (2006) 161–164, https://doi.org/10.1107/S0108768105030570.

[35] J. Skelton, Transformer, Https://Github.Com/JMSkelton/Transformer. (n.d.).

[36] T.J. Chung, J.S. Lee, D.Y. Kim, G.H. Kim, H. Song, Morphology and phase stability of nitrogen-partially stabilized zirconia (N-PSZ), J. Am. Ceram. Soc. 84 (2001) 172–178, https://doi.org/10.1111/j.1151-2916.2001.tb00626.x.

[37] C. Wang, M. Zinkevich, F. Aldinger, On the thermodynamic modeling of the Zr–O system, Calphad 28 (2004) 281–292, https://doi.org/10.1016/j.calphad.2004.09.002.

[38] L. Gribaudo, D. Arias, J. Abriata, The N-Zr (Nitrogen-Zirconium) System, J. Phase Equilibria. 15 (1994) 441–449, https://doi.org/10.1007/BF02647575.

[39] R.J. McCabe, G. Proust, E.K. Cerreta, A. Misra, Quantitative analysis of deformation twinning in zirconium, Int. J. Plast. 25 (2009) 454–472, https://doi.org/10.1016/j.ijplas.2008.03.010.

[40] W. Guo, G. Li, F. Yuan, F. Han, Y. Zhang, M. Ali, J. Ren, G. Yuan, Texture development and mechanical behavior of Zircaloy-4 alloy plates fabricated by cold rolling and annealing, Mater. Sci. Eng. A. 807 (2021) 140846, https://doi.org/10.1016/j.msea.2021.140846.

[41] J. Romero, M. Preuss, J. Quinta da Fonseca, Texture memory and variant selection during phase transformation of a zirconium alloy, Acta Mater. 57 (2009) 5501–5511, https://doi.org/10.1016/j.actamat.2009.07.046.

[42] A.R. Massih, L.O. Jernkvist, Solid state phase transformation kinetics in Zr-base alloys, Sci. Rep. 11 (2021) 7022, https://doi.org/10.1038/s41598-021-86308-w.

[43] J.S. Foord, P.J. Goddard, R.M. Lambert, Adsorption and absorption of diatomic gases by zirconium: Studies of the dissociation and diffusion of CO, NO, N2, O2 and D2, Surf. Sci. 94 (1980) 339–354, https://doi.org/10.1016/0039-6028(80)90011-4.

[44] S. Kirklin, J.E. Saal, B. Meredig, A. Thompson, J.W. Doak, M. Aykol, S. Rühl, C. Wolverton, The Open Quantum Materials Database (OQMD): Assessing the accuracy of DFT formation energies, NPJ Comput. Mater. 1 (2015) 15010, https://doi.org/10.1038/npjcompumats.2015.10.

[45] P.D.L. Mercera, J.G. van Ommen, E.B.M. Doesburg, A.J. Burggraaf, J.R.H. Roes, Stabilized tetragonal zirconium oxide as a support for catalysts Evolution of the texture and structure on calcination in static air, Appl. Catal. 78 (1991) 79–96, https://doi.org/10.1016/0166-9834(91)80090-J.

[46] V.T. Veettil, M. Mohankumar, D. Zitoun, Site-engineered tetragonal ZrO 2 nanoparticles: a promising oxygen reduction catalyst with high activity and chemical stability in alkaline medium, Adv. Mater. Interfaces 9 (2022) 2101802, https://doi.org/10.1002/admi.202101802.

[47] M. Steinbrück, High-temperature reaction of oxygen-stabilized α-Zr(O) with nitrogen, J. Nucl. Mater. 447 (2014) 46–55, https://doi.org/10.1016/j.jnucmat.2013.12.024.

[48] Y. Ikuma, A. Shoji, High temperature oxidation of ZrN powder in oxygen atmosphere. Adv. Mater. '93, Elsevier, 1994, pp. 277–280, https://doi.org/10.1016/b978-0-444-81991-8.50074-1.

[49] R.W. Harrison, W.E. Lee, Mechanism and kinetics of oxidation of ZrN ceramics, J. Am. Ceram. Soc. 98 (2015) 2205–2213, https://doi.org/10.1111/jace.13575.

[50] D. Simeone, G. Baldinozzi, D. Gosset, M. Dutheil, A. Bulou, T. Hansen, Monoclinic to tetragonal semireconstructive phase transition of zirconia, Phys. Rev. B. 67 (2003) 064111, https://doi.org/10.1103/PhysRevB.67.064111.

[51] P. Platt, P. Frankel, M. Gass, R. Howells, M. Preuss, Finite element analysis of the tetragonal to monoclinic phase transformation during oxidation of zirconium alloys, J. Nucl. Mater. 454 (2014) 290–297, https://doi.org/10.1016/j.jnucmat.2014.08.020.

[52] W. Qin, C. Nam, H.L. Li, J.A. Szpunar, Tetragonal phase stability in ZrO2 film formed on zirconium alloys and its effects on corrosion resistance, Acta Mater. 55 (2007) 1695–1701, https://doi.org/10.1016/j.actamat.2006.10.030.
[53] M. Steinbrück, Prototypical experiments relating to air oxidation of Zircaloy-4 at high temperatures, J. Nucl. Mater. 392 (2009) 531–544, https://doi.org/10.1016/j.jnucmat.2009.04.018.
[54] R. Guillou, M. Le Saux, E. Rouesne, D. Hamon, C. Toffolon-Masclet, D. Menut, J. C. Brachet, J.L. Béchade, D. Thiaudière, In-situ time-resolved study of structural evolutions in a zirconium alloy during high temperature oxidation and cooling, Mater. Charact. 158 (2019) 109971, https://doi.org/10.1016/j.matchar.2019.109971.
[55] N. Pétigny, P. Barberis, C. Lemaignan, C. Valot, M. Lallemant, In situ XRD analysis of the oxide layers formed by oxidation at 743 K on Zircaloy 4 and Zr–1NbO, J. Nucl. Mater. 280 (2000) 318–330, https://doi.org/10.1016/S0022-3115(00)00051-9.
[56] J. Liao, Z. Yang, S. Qiu, Q. Peng, Z. Li, J. Zhang, The correlation between tetragonal phase and the undulated metal/oxide interface in the oxide films of zirconium alloys, J. Nucl. Mater. 524 (2019) 101–110, https://doi.org/10.1016/j.jnucmat.2019.06.039.
[57] M. Le Saux, J.-C. Brachet, V. Vandenberghe, A. Ambard, R. Chosson, Breakaway oxidation of zirconium alloys exposed to steam around 1000 °C, Corros. Sci. 176 (2020) 108936, https://doi.org/10.1016/j.corsci.2020.108936.
[58] M. Steinbrück, High-temperature oxidation of zirconium alloys in various atmospheres. Encycl. Mater. Met. Alloy., Elsevier, 2022, pp. 454–463, https://doi.org/10.1016/B978-0-12-819726-4.00006-5.
[59] A. Bouayoune, R. Guillou, J.-L. Béchade, E. Rouesne, D. Thiaudière, J.-L. Grosseau-Poussard, B. Panicaud, M. Le Saux, Study of the evolution of stresses and associated mechanisms in zirconia growing at high temperature on Zircaloy-4 by use of synchrotron radiation, Corros. Sci. 221 (2023) 111328, https://doi.org/10.1016/j.corsci.2023.111328.